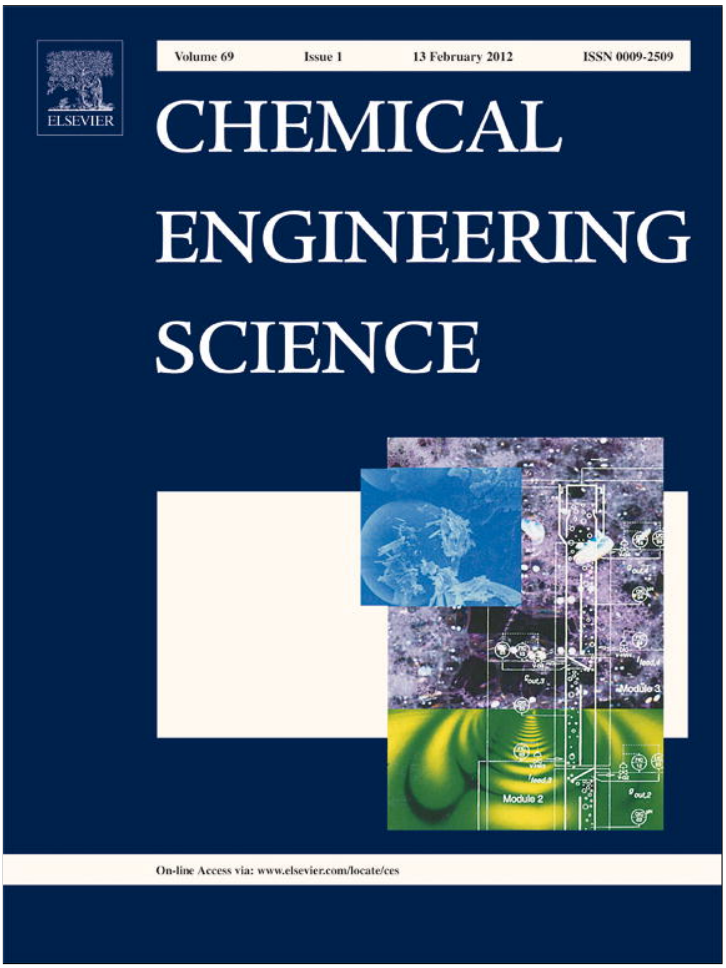

Chemical Engineering Science 69 (2012) 59–68

Contents lists available at SciVerse ScienceDirect

Chemical Engineering Science

journal homepage: www.elsevier.com/locate/ces

An operator-splitting finite element method for the efficient parallel solution of multidimensional population balance systems

Sashikumaar Ganesan [a,*], Lutz Tobiska [b]

[a] Numerical Mathematics and Scientific Computing, Supercomputer Education and Research Centre, Indian Institute of Science, Bangalore 560012, India
[b] Institute of Analysis and Numerical Mathematics, Otto-von-Guericke University, PF 4120 D-39016 Magdeburg, Germany

ARTICLE INFO

Article history:
Received 12 April 2011
Received in revised form
20 August 2011
Accepted 14 September 2011
Available online 22 September 2011

Keywords:
Population balance
Crystallization
Mathematical modeling
Finite elements
Operator-splitting
Simulation

ABSTRACT

A finite element method for solving multidimensional population balance systems is proposed where the balance of fluid velocity, temperature and solute partial density is considered as a two-dimensional system and the balance of particle size distribution as a three-dimensional one. The method is based on a dimensional splitting into physical space and internal property variables. In addition, the operator splitting allows to decouple the equations for temperature, solute partial density and particle size distribution. Further, a nodal point based parallel finite element algorithm for multi-dimensional population balance systems is presented. The method is applied to study a crystallization process assuming, for simplicity, a size independent growth rate and neglecting agglomeration and breakage of particles. Simulations for different wall temperatures are performed to show the effect of cooling on the crystal growth. Although the method is described in detail only for the case of $d=2$ space and $s=1$ internal property variables it has the potential to be extendable to $d+s$ variables, $d=2$, 3 and $s\geq 1$.

1. Introduction

Crystallization is one of the main processes in many chemical and pharmaceutical industries (Hulburt and Katz, 1964; Woo et al., 2009). The understanding of the crystallization process is very important in order to improve the product quality and to minimize the production cost. In general, the properties of the product crystals mainly depend on the particulate characteristics (Teipel, 2004). Thus, to understand the crystallization process better and to predict the properties of the particles in advance, modeling and simulation of crystallization processes is highly demanded. The particle size (typically the characteristic length, volume or mass) distribution (PSD) in particulates is best described by population balance equations (PBEs) (Ramkrishna, 2000). Further, to incorporate the effects of non-ideal mixing in the crystallizer on the population balance model, the PBE has to be coupled with the flow (Chen et al., 2004; Hulburt and Katz, 1964; Lian et al., 2006). The coupled system of equations which describe the crystallization process in a non-ideal mixing crystallizer is often called as a population balance system (John et al., 2009). A population balance system (PBS) typically consists of the time-dependent Navier–Stokes equations to describe the flow field, a couple of nonlinear convection–diffusion–reaction equations for describing chemical reactions, transport of temperature or concentrations, and a multidimensional PBE to describe the PSD. In general, the PBE contains derivatives with respect to four or more coordinates (three spatial coordinates and one or more internal property coordinates). Thus, the PBE is posed on a higher dimensional domain compared to the other equations in the PBS.

Simulation of a non-ideal mixing crystallization process consists of solving a set of strongly coupled multidimensional partial differential equations. Apart from the other challenges associated with the solution of the multidimensional PBE, coupling the PBE with the Navier–Stokes and scalar equations makes the solution process more challenging (Woo et al., 2006). Even though many accurate methods are available for the solution of partial differential equations, their use for population balance systems is lacking. The numerical solution of the PBE is itself very challenging, and is an active field of research (Ramkrishna and Mahoney, 2002). A number of specialised numerical schemes for the solution of PBE has been proposed in the literature, for an overview see, Braatz (2002), Costa et al. (2007), Gunawan et al. (2004), Ramkrishna (2000) and the references therein. Each method has its own advantages and disadvantages, and here we focus only on the most relevant discretization methods.

Finite difference method was one of the popular discretization methods for the PBE. It has been used by several authors for different particulate systems, for an overview, see Gunawan et al. (2004),

* Corresponding author.
E-mail addresses: sashi@serc.iisc.ac.in (S. Ganesan), tobiska@ovgu.de (L. Tobiska).
URLS: http://www.serc.iisc.ernet.in/~sashi/ (S. Ganesan), http://www-ian.math.uni-magdeburg.de/home/tobiska (L. Tobiska).

0009-2509/$ - see front matter © 2011 Elsevier Ltd. All rights reserved.
doi:10.1016/j.ces.2011.09.031

Pinto et al. (2008), Ramkrishna (2000) and the references therein. Finite difference method is simple to apply and easy to extend for multidimensional equations, see the recent works of Hackbusch et al. (in press) and John and Roland (2010) for its application to 4D PBEs. However, the finite difference cannot be applied when the computational domain of the multidimensional PBE is complex, especially the spatial coordinate domain.

An alternative approach to use the high-resolution finite volume method has been proposed in Ma et al. (2002a). The basic idea in this approach is to apply the dimensional splitting to the multidimensional PBE to obtain a set of one-dimensional (1D) equations and solve each 1D equation using the high-resolution finite volume method. This approach avoids smearing and spurious oscillations in the numerical solution of the PBE. Numerous variants of the high-resolution finite volume algorithms and their applications to different particulate systems have been proposed and used by several authors, see for example Gunawan et al. (2004), Ma et al. (2002b), Majumder et al. (2010), Qamar et al. (2007, 2011), and Woo et al. (2009). A parallel implementation of this method has been proposed in Gunawan et al. (2008) with a special technique to avoid improper load balance, which occurs because of varying computational load across the internal grid cells in the evaluation of source–sink integral terms (*e.g.*, aggregation and breakage) in the PBE.

Recently, a finite element approach based on the dimensional splitting has been proposed in Ganesan (2010) and Ganesan and Tobiska (2011) for high-dimensional equations of population balance type. In contrast to the splitting applied (split into a set of 1D equations) to the PBE in Gunawan et al. (2004), only two operator-split equations (spatial and internal) are obtained in the finite element approach. Here, the spatial (typically 3D) and internal (1D or more) contain all derivatives with respect to the spatial and internal coordinates, respectively. An advantage of this splitting approach is that the shape of the spatial domain (crystallizer) can be arbitrary and the spatial equation can be easily incorporated into the CFD model. Another advantage is that it is enough to decompose the spatial domain in the parallel implementation. This domain decomposition does not need a special technique for load balancing in parallel implementations as in Gunawan et al. (2008), since the internal grid is not decomposed. Further, in this paper we apply the splitting also to the coupled scalar (energy and component mass balance) equations and obtain a system of uncoupled partial differential equations (PDEs) and coupled ordinary differential equations (ODEs). This facilitates to apply the decoupling iteration only between a set of ODEs and operator-split internal PBE equation.

2. Population balance systems

2.1. Model assumptions

We consider modeling of crystallization process, which occurs due to cooling. Since our main focus is to develop an accurate and robust numerical scheme for population balance systems, we neglect gravitational effects, agglomeration and breakage of particles. In addition, we assume that the liquid solvent is incompressible, the fluid flow is stationary, the fluid properties such as density, kinematic viscosity, heat conductivity and specific heat are spatially uniform (John et al., 2009; Hackbusch et al., in press). Using the density and effective viscosity of the suspension would be appropriate for PBS (Chang and Powell, 2002; Woo et al., 2006). However, it requires additional efforts mainly in the Navier–Stokes solver, and here the focus is on a finite element scheme for solving the multidimensional PBE coupled with the mass and momentum equations. Thus, for simplicity we made these assumptions.

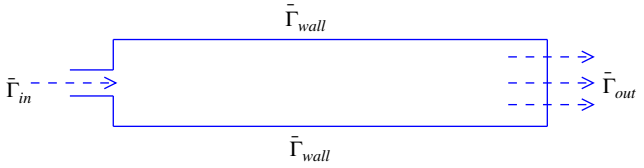

Fig. 1. The computational spatial domain $\Omega_{\overline{X}}$ for the crystallization process. Here, the $\overline{\Gamma}_{in}$ is the fluid inlet, $\overline{\Gamma}_{out}$ is the fluid outlet and $\overline{\Gamma}_{wall} := \partial\Omega_{\overline{X}} \backslash (\overline{\Gamma}_{in} \cup \overline{\Gamma}_{out})$ is the container wall.

A two-dimensional (2D) spatial space and an 1D internal space, *i.e.*, one internal property coordinate, say the crystal particle size distribution are considered. We mimic the experimental setup used in Borchert and Sundmacher (2011), and Fig. 1 gives a schematic view of the considered 2D crystallizer (spatial domain $\Omega_{\overline{X}} \subset \mathbb{R}^2$), which is 2 m in length and 1×10^{-2} m in width. The inlet and outlet boundaries of the crystallizer are denoted by $\overline{\Gamma}_{in}$ and $\overline{\Gamma}_{out}$, respectively, whereas the remaining boundary parts are denoted as $\overline{\Gamma}_{wall}$, *i.e.*, $\overline{\Gamma}_{wall} := \partial\Omega_{\overline{X}} \backslash (\overline{\Gamma}_{in} \cup \overline{\Gamma}_{out})$. We assume that the minimum size of the particles injected into the crystallizer is 2.5×10^{-6} m and the maximum possible particle size is 1.69×10^{-3} m. Thus, our internal domain will be $\Omega_{\overline{L}} := (\overline{L}_{min}, \overline{L}_{max}) = (2.5 \times 10^{-6}\ \text{m}, 1.69 \times 10^{-3}\ \text{m})$.

2.2. Governing equations

In the considered population balance system, the stationary flow field of the solute in the bounded spatial domain $\Omega_{\overline{X}}$ is described by the stationary incompressible Navier–Stokes equations

$$\nabla \cdot \overline{\mathbf{u}} = 0, \quad \rho(\overline{\mathbf{u}} \cdot \nabla)\overline{\mathbf{u}} + \nabla \overline{p} = \mu \Delta \overline{\mathbf{u}} \ \text{ in } \Omega_{\overline{X}}, \tag{1}$$

where $\overline{\mathbf{u}} = (\overline{u}_1, \overline{u}_2)$ is the fluid velocity, $\overline{p}$ is the pressure, ρ and μ are the density and dynamic viscosity of the fluid, respectively. Further, ∇, $\nabla\cdot$ and Δ denote the gradient, divergence and Laplace operators with respect to the spatial variables $\overline{\mathbf{x}} = (\overline{x}_1, \overline{x}_2) \in \Omega_{\overline{X}}$, respectively. The Navier–Stokes equations (1) are closed with the following boundary conditions:

$$\overline{\mathbf{u}} = \overline{\mathbf{u}}_D \quad \text{on } \overline{\Gamma}_{in},$$

$$\overline{\mathbf{u}} = 0 \quad \text{on } \overline{\Gamma}_{wall},$$

$$\mu \frac{\partial \overline{\mathbf{u}}}{\partial n} - \overline{p} n = 0 \quad \text{on } \overline{\Gamma}_{out}.$$

Here, $\overline{\mathbf{u}}_D$ is a given velocity and n is the outward normal to the boundary $\overline{\Gamma}_{out}$. Together with the Navier–Stokes equations (1), the population balance system consists of the time-dependent 2D energy and mass balance equations of the solute, and a three-dimensional (3D) population balance equation for the size distribution of the crystal particles. In the given time interval $(0, \overline{T}]$, the equation for the energy balance reads

$$\rho c_p \left(\frac{\partial \overline{\vartheta}}{\partial \overline{t}} + \overline{\mathbf{u}} \cdot \nabla \overline{\vartheta} \right) = \lambda \Delta \overline{\vartheta} + h_{cr} H_{gr} \quad \text{in } (0, \overline{T}] \times \Omega_{\overline{X}}, \tag{2}$$

with the boundary and initial conditions

$$\overline{\vartheta} = \vartheta_D \quad \text{on } (0, \overline{T}] \times \overline{\Gamma}_{in},$$

$$\overline{\vartheta} = \vartheta_{wall} \quad \text{on } (0, \overline{T}] \times \overline{\Gamma}_{wall},$$

$$\frac{\partial \overline{\vartheta}}{\partial n} = 0 \quad \text{on } (0, \overline{T}] \times \overline{\Gamma}_{out},$$

$$\overline{\vartheta}(0, \cdot) = \vartheta_0 \quad \text{in } \Omega_{\overline{X}}.$$

Here, $\overline{t} \in (0,\overline{T}]$ is the time, $\overline{\vartheta}$ denotes the temperature, c_p the heat capacity, λ the thermal conductivity, h_{cr} the heat of solution, ϑ_0 the initial value of $\overline{\vartheta}$, ϑ_D and ϑ_{wall} are given boundary values of the temperature with $\vartheta_{wall} \le \vartheta_D$. Next, a component mass balance equation for the solute partial density in $(0,T]$ is given by

$$\frac{\partial \overline{\rho}_c}{\partial \overline{t}} + \overline{\mathbf{u}} \cdot \nabla \overline{\rho}_c = D_c \Delta \overline{\rho}_c + H_{gr} \quad \text{in } (0,\overline{T}] \times \Omega_{\overline{X}}, \tag{3}$$

with the boundary and initial conditions

$$\overline{\rho}_c = \rho_{c_D} \quad \text{on } (0,\overline{T}] \times \overline{\Gamma}_{in},$$

$$\frac{\partial \overline{\rho}_c}{\partial n} = 0 \quad \text{on } (0,\overline{T}] \times (\overline{\Gamma}_{wall} \cup \overline{\Gamma}_{out}),$$

$$\overline{\rho}_c(0,\cdot) = \rho_{c_0} \quad \text{in } \Omega_{\overline{X}}.$$

Here, the source term H_{gr}, which accounts for the mass transfer is given by

$$H_{gr}(\overline{\vartheta},\overline{\rho}_c,\overline{f}) = -3\rho^d k_V G \int_{\Omega_{\overline{L}}} \overline{\ell}^2 \overline{f}\, d\overline{\ell},$$

where the growth rate G is given by

$$G(\overline{\rho}_c,\overline{\vartheta}) = \begin{cases} k_g \left(\dfrac{\overline{\rho}_c - \rho_{c,sat}(\overline{\vartheta})}{\rho_{c,sat}(\overline{\vartheta})} \right)^g & \text{if } \overline{\rho}_c > \rho_{c,sat}(\overline{\vartheta}), \\ 0 & \text{else.} \end{cases}$$

In the above equations, $\overline{\rho}_c$ denotes the solute partial density which is a source for the crystal growth, D_c the diffusion coefficient of the solute partial density, ρ^d the density of the crystal. Further, ρ_{c_0} is the initial values of $\overline{\rho}_c$, k_V the shape factor, g the growth exponent, k_g the growth factor and $c_D = \rho_{c,sat}(\vartheta_D)$ are given values. An empirical expression for the saturation concentration $\rho_{c,sat}$ is given by

$$\rho_{c,sat}(\overline{\vartheta}) = 1.3045(\overline{\vartheta} - 273.15) + 35.3642$$

based on the experimental studies presented in Krasnyk et al. (in press-a). Finally, the governing equation for the particle size distribution of the dispersed particle phase which accounts for the crystal growth and the convective transport in the spatial space is given by

$$\frac{\partial \overline{f}}{\partial \overline{t}} + \overline{\mathbf{u}} \cdot \nabla \overline{f} + G \frac{\partial \overline{f}}{\partial \overline{\ell}} = D_x \Delta \overline{f} \quad \text{in } (0,\overline{T}] \times \Omega_{\overline{X}} \times \Omega_{\overline{L}}, \tag{4}$$

with the boundary and initial conditions

$$\frac{\partial \overline{f}}{\partial n} = 0 \quad \text{on } (0,\overline{T}] \times (\overline{\Gamma}_{wall} \cup \overline{\Gamma}_{out}) \times (\overline{\Omega}_{\overline{L}} \backslash \overline{L}_{min}),$$

$$\overline{f} = f_D \quad \text{on } (0,\overline{T}] \times \overline{\Gamma}_{in} \times \overline{\Omega}_{\overline{L}},$$

$$\overline{f} = \frac{B_{nuc}}{G} \quad \text{on } (0,\overline{T}] \times (\overline{\Omega}_{\overline{X}} \backslash \overline{\Gamma}_{in}) \times \overline{L}_{min},$$

$$\overline{f}(0,\cdot,\cdot) = f_0 \quad \text{in } \Omega_{\overline{X}} \times \Omega_{\overline{L}}.$$

Here, $\overline{f}$ denotes the particle size distribution, D_x the artificial diffusion coefficient of the particles, f_D denotes the particle size distribution of the feed crystals. Further, the nucleation rate B_{nuc} is defined as

$$B_{nuc} = \alpha_{nuc} \exp\left(\frac{-\beta_{nuc}}{\ln^2(\overline{\rho}_c / \rho_{c,sat}(\overline{\vartheta}))} \right),$$

where α_{nuc} is the nucleation constant and β_{nuc} is a model constant.

2.3. Dimensionless problem

In this section we derive the dimensionless form of the population balance system, Eqs. (1)–(4). Let us introduce the scaling factors X and L as characteristic lengths of the spatial space and internal space, respectively, and U as the characteristic velocity. Further, we define the non-dimensional variables as

$$\mathbf{x} = \frac{\overline{\mathbf{x}}}{X}, \quad \ell = \frac{\overline{\ell}}{L}, \quad t = \frac{\overline{t}U}{X}, \quad \mathbf{u} = \frac{\overline{\mathbf{u}}}{U},$$

$$p = \frac{\overline{p}}{\rho U^2}, \quad L_{min} = \frac{\overline{L}_{min}}{L}, \quad L_{max} = \frac{\overline{L}_{max}}{L},$$

$$\vartheta = \frac{\overline{\vartheta}}{\vartheta_D}, \quad \rho_c = \frac{\overline{\rho}_c}{\rho_{c_D}}, \quad f = \frac{\overline{f}}{f_{max}}.$$

Here, f_{max} is the possible maximum value of $\overline{f}$ over the time. In addition, the Reynolds and Péclet numbers are defined as

$$Re = \frac{\rho X U}{\mu}, \quad Pe_\vartheta = \frac{XU}{\sigma},$$

$$Pe_c = \frac{XU}{D_c}, \quad Pe_x = \frac{XU}{D_x},$$

where $\sigma = \lambda/\rho c_p$ is the thermal diffusivity. Using these dimensionless variables and numbers in Eqs. (1)–(4), in $(0,T]$ with $T = \overline{T}U/X$, we get the following dimensionless form of the population balance system:

$$(\mathbf{u} \cdot \nabla)\mathbf{u} + \nabla p = \frac{1}{Re} \Delta \mathbf{u} \quad \nabla \cdot \mathbf{u} = 0 \text{ in } \Omega_X, \tag{5}$$

$$\frac{\partial \vartheta}{\partial t} + \mathbf{u} \cdot \nabla \vartheta = \frac{1}{Pe_\vartheta} \Delta \vartheta + H_{gr}^{\vartheta} \quad \text{in } (0,T] \times \Omega_X, \tag{6}$$

$$\frac{\partial \rho_c}{\partial t} + \mathbf{u} \cdot \nabla \rho_c = \frac{1}{Pe_c} \Delta \rho_c + H_{gr}^{\rho} \quad \text{in } (0,T] \times \Omega_X, \tag{7}$$

$$\frac{\partial f}{\partial t} + \mathbf{u} \cdot \nabla f + \frac{X}{UL} G \frac{\partial f}{\partial \ell} = \frac{1}{Pe_x} \Delta f \quad \text{in } (0,T] \times \Omega_X \times \Omega_L. \tag{8}$$

Here, Ω_X and Ω_L denote the scaled domains of $\Omega_{\overline{X}}$ and $\Omega_{\overline{L}}$, respectively. The dimensionless source terms $H_{gr}^{\vartheta}(\vartheta,\rho_c,f)$ and $H_{gr}^{\rho}(\vartheta,\rho_c,f)$ in the energy and the mass balance are given by

$$H_{gr}^{\vartheta} = -3\rho^d k_V h_{cr} \frac{XL^3 f_{max}}{U \rho c_p \vartheta_D} G(\rho_c,\vartheta) \int_{\Omega_L} \ell^2 f\, d\ell,$$

$$H_{gr}^{\rho} = -3\rho^d k_V \frac{XL^3 f_{max}}{U c_D} G(\rho_c,\vartheta) \int_{\Omega_L} \ell^2 f\, d\ell.$$

In the above population balance system, the Navier–Stokes, the energy and the mass balance equations (5)–(7) contain derivatives with respect to $\mathbf{x} \in \Omega_X$, whereas the population balance equation (8) contains derivatives with respect to $\mathbf{x} \in \Omega_X$ as well as $\ell \in \Omega_L$. Further, the energy equation (6), the mass balance equation (7) and the population balance equation (8) are coupled through the source term.

3. Numerical scheme

3.1. Operator-splitting finite element method

The stationary Navier–Stokes equations are solved once, and the stationary velocity is used in the convective terms of all time-dependent scalar equations (6)–(8). The two main challenges associated with the solution of the scalar equations are (i) the coupling between the equations in 2D and 3D domains, and (ii) the higher-dimension of the population balance equation. We overcome

these difficulties by applying an operator-splitting. In our approach, advancing the solution in time consists of two steps. In the first step, the gradient and Laplace operators depend on spatial coordinates $\mathbf{x} \in \Omega_X$ will be considered, whereas in the second step the coupling and growth terms will be considered.

Let $0 = t^0 < t^1 < \cdots < t^N = T$ be a decomposition of the considered time interval $[0, T]$. Let us denote $\tau = t^n - t^{n-1}$, $1 \le n \le N$, be a sequence of uniform time steps. For brevity we use the superscript n to denote a variable at time t^n, for example $\vartheta^n(\mathbf{x}) := \vartheta(t^n,\mathbf{x})$. Now, using the operator-splitting finite element method in the time interval (t^{n-1},t^n), we split the coupled multi-dimensional system of equations (6)–(8) into two subproblems, one in X-direction and another in L-direction:

X-direction (*Step*1): For given $\hat{\vartheta}^{n-1} = \vartheta(t^{n-1},\mathbf{x})$, $\hat{\rho}_c^{n-1} = \rho_c(t^{n-1},\mathbf{x})$ and $\hat{f}^{n-1} = f(t^{n-1},\mathbf{x},\ell)$, find $\hat{\vartheta}$, $\hat{\rho}_c$ and $\hat{f}$ in (t^{n-1},t^n) such that for all $\ell \in (L_{min},L_{max}]$

$$\frac{\partial \hat{\vartheta}}{\partial t} + \mathbf{u}\cdot\nabla\hat{\vartheta} = \frac{1}{Pe_\vartheta}\Delta\hat{\vartheta} \quad \text{in } \Omega_X,$$

$$\frac{\partial \hat{\rho}_c}{\partial t} + \mathbf{u}\cdot\nabla\hat{\rho}_c = \frac{1}{Pe_C}\Delta\hat{\rho}_c \quad \text{in } \Omega_X,$$

$$\frac{\partial \hat{f}}{\partial t} + \mathbf{u}\cdot\nabla\hat{f} = \frac{1}{Pe_x}\Delta\hat{f} \quad \text{in } \Omega_X, \tag{9}$$

and

$$\hat{\vartheta} = 1, \quad \hat{\rho}_c = 1, \quad \hat{f} = \frac{f_D}{f_{max}} \text{ on } \Gamma_{in},$$

$$\hat{\vartheta} = \frac{\vartheta_{wall}}{\vartheta_D}, \quad \frac{\partial \hat{\rho}_c}{\partial n} = 0, \quad \frac{\partial \hat{f}}{\partial n} = 0 \text{ on } \Gamma_{wall},$$

$$\frac{\partial \hat{\vartheta}}{\partial n} = 0, \quad \frac{\partial \hat{\rho}_c}{\partial n} = 0, \quad \frac{\partial \hat{f}}{\partial n} = 0 \text{ on } \Gamma_{out}.$$

Here, Γ_{in}, Γ_{out} and Γ_{wall} are scaled boundary parts of $\overline{\Gamma}_{in}$, $\overline{\Gamma}_{out}$ and $\overline{\Gamma}_{wall}$, respectively.

L-direction (*Step*2): For given $\tilde{\vartheta}^{n-1} = \hat{\vartheta}^n$, $\tilde{\rho}_c^{n-1} = \hat{\rho}_c^n$, and $\tilde{f}^{n-1} = \hat{f}^n$, find $\tilde{\vartheta}$, $\tilde{\rho}_c$ and $\tilde{f}$ in (t^{n-1},t^n) such that for all $\mathbf{x} \in \overline{\Omega}_X \backslash \Gamma_{in}$

$$\frac{d\tilde{\vartheta}}{dt} - H_{gr}^{\vartheta}(\tilde{\vartheta},\tilde{\rho}_c,\tilde{f}) = 0,$$

$$\frac{d\tilde{\rho}_c}{dt} - H_{gr}^{\rho}(\tilde{\vartheta},\tilde{\rho}_c,\tilde{f}) = 0,$$

$$\frac{\partial \tilde{f}}{\partial t} + \frac{X}{UL}G\frac{\partial \tilde{f}}{\partial \ell} = 0 \quad \text{in } \Omega_L,$$

$$\tilde{f}(t,\mathbf{x},L_{min}) = \frac{1}{f_{max}}\frac{B_{nuc}}{G}. \tag{10}$$

Note that in the first step (9), the energy, the mass and the population balance equations are decoupled. Moreover, all equations live on the same 2D spatial domain Ω_X. In the first step, the energy and mass balance equations have to be solved once, whereas the population balance equation has to be solved for all $\ell \in \Omega_L$ by considering ℓ as a parameter. In the second step (10), for all $\mathbf{x} \in \overline{\Omega}_X \backslash \Gamma_{in}$, two ODEs and an 1D PDE have to be solved. Further, an iterative procedure is needed when the coupled equations (10) are solved implicitly. However, the iterative procedure will not be expensive as it is applied to an 1D (internal space) PDE and ODEs.

3.2. Discrete form of the operator-split system

Let $V := H^1(\Omega_X)$, $Q := H^1(\Omega_L)$ be the usual Sobolev spaces. Further, let

$$W_0 := \{\phi \in V : \phi = 0 \text{ on } \Gamma_{in} \cup \Gamma_{wall}\},$$

$$V_0 := \{\phi \in V : \phi = 0 \text{ on } \Gamma_{in}\},$$

$$Q_0 := \{\psi \in Q : \psi(L_{min}) = 0\}.$$

Suppose $V_h \subset V$, $Q_h \subset Q$, $V_{0,h} \subset V_0$, $W_{0,h} \subset W_0$ and $Q_{0,h} \subset Q_0$ are conforming finite element spaces. Define finite element functions $\hat{\vartheta}_h^n(\mathbf{x}) \in V_h$, $\hat{\rho}_{c,h}^n(\mathbf{x}) \in V_h$ $\hat{f}_h^n(\cdot,\ell_l) \in V_h$ and $\tilde{f}_h^n(\mathbf{x}_j,\cdot) \in Q_h$ as

$$\hat{\vartheta}_h^n(\mathbf{x}) := \sum_{j=1}^{\mathcal{M}} \hat{\vartheta}_j^n \phi_j(\mathbf{x}), \quad \hat{\rho}_{c,h}^n(\mathbf{x}) := \sum_{j=1}^{\mathcal{M}} \hat{\rho}_j^n \phi_j(\mathbf{x}),$$

$$\hat{f}_h^n(\mathbf{x},\ell_l) := \sum_{j=1}^{\mathcal{M}} \hat{f}_{j,l}^n \phi_j(\mathbf{x}),$$

$$\tilde{f}_h^n(\mathbf{x}_j,\ell) := \sum_{l=1}^{\mathcal{N}} \tilde{f}_{j,l}^n \psi_l(\ell).$$

Here, $\mathcal{M}$, ϕ_j and $\mathcal{N}$, ψ_l are the number of degrees of freedom, the basis functions of V_h and Q_h, respectively. Further, to retrieve the global discrete solution of f, we define $V_h \otimes Q_h \subset H^{1,1}(\Omega)$ as

$$V_h \otimes Q_h = \left\{ \xi_h : \xi_h = \sum_{i=1}^{\mathcal{M}} \sum_{k=1}^{\mathcal{N}} \xi_{i,k}\phi_i\psi_k; \xi_{i,k} \in \mathbb{R} \right\},$$

where

$$H^{1,1}(\Omega) := H^1(\Omega_X; H^1(\Omega_L)) \cap H^1(\Omega_L; H^1(\Omega_X)).$$

Here, the Sobolev space $H^{1,1}(\Omega)$ is slightly more regular than the standard space $H^1(\Omega)$, where the mixed partial derivatives are bounded (Ganesan, 2010; Ganesan and Tobiska, 2011).

In order to apply the nodal point based operator-splitting algorithm (Ganesan and Tobiska, 2011), let $\mathbf{x}_j \in \Omega_X$, $j = 1,\ldots,N\_XP$, and $\ell_l \in \Omega_L$, $l = 1,\ldots,N\_LP$ be the Cartesian coordinates which are necessary to evaluate nodal functionals of the finite element spaces V_h and Q_h, respectively. Now, we apply the spatial and the backward Euler discretizations in space and time, respectively, to the operator-split equations in (9) and (10). In (t^{n-1},t^n), the discrete forms of the energy, mass and population balance in the first step of the operator-splitting scheme read

X-direction (*Step*1): For given $\hat{\vartheta}_h^{n-1} = \vartheta_h^{n-1}$, $\hat{\rho}_{c,h}^{n-1} = \rho_{c,h}^{n-1}$ and $\hat{f}_h^{n-1} = f_h^{n-1}$, find $\hat{\vartheta}_h^n \in V_h$, $\hat{\rho}_{c,h}^n \in V_h$ and $\hat{f}_h^n \in V_h$ such that for $l = 1,\ldots,N\_LP$,

$$\begin{aligned}
&(\partial_\tau \hat{\vartheta}_h^n, \phi_h)_X + \frac{1}{Pe_\vartheta}(\nabla\hat{\vartheta}_h^n, \nabla\phi_h)_X + (\mathbf{u}_h\cdot\nabla\hat{\vartheta}_h^n, \phi_h)_X = 0, \quad \forall \phi_h \in W_{0,h},\\
&(\partial_\tau \hat{\rho}_{c,h}^n, \phi_h)_X + \frac{1}{Pe_C}(\nabla\hat{\rho}_{c,h}^n, \nabla\phi_h)_X + (\mathbf{u}_h\cdot\nabla\hat{\rho}_{c,h}^n, \phi_h)_X = 0, \quad \forall \phi_h \in V_{0,h},\\
&(\partial_\tau \hat{f}_h^n, \phi_h)_X + \frac{1}{Pe_x}(\nabla\hat{f}_h^n, \nabla\phi_h)_X + (\mathbf{u}_h\cdot\nabla\hat{f}_h^n, \phi_h)_X = 0, \quad \forall \phi_h \in V_{0,h},
\end{aligned} \tag{11}$$

where $\partial_\tau g^n = (g^n - g^{n-1})/\tau$ for a function g. Further, the inner product in $L^2(\Omega_{X,h})$ is denoted by $(\cdot,\cdot)_X$.

Similarly, the discrete form of the equations in the second step of the operator-splitting scheme read:

L-direction (*Step*2): For given $\tilde{\vartheta}_h^{n-1} = \hat{\vartheta}_h^n$, $\tilde{\rho}_{c,h}^{n-1} = \hat{\rho}_{c,h}^n$ and $\tilde{f}_h^{n-1} = \hat{f}_h^n$, find $\tilde{\vartheta}_h^n \in V_h$, $\tilde{\rho}_c^n \in V_h$ and $\tilde{f}_h^n \in Q_h$ such that for $j = 1,\ldots,N\_XP$,

$$\partial_\tau \tilde{\vartheta}_h^n - H_{gr}^{\vartheta}(\tilde{\vartheta}_h^n, \tilde{\rho}_{c,h}^n, \tilde{f}_h^n) = 0,$$

$$\partial_\tau \tilde{\rho}^n_{c,h} - H^\rho_{gr}(\tilde{\vartheta}^n_h, \tilde{\rho}^n_{c,h}, \tilde{f}^n_h) = 0,$$

$$(\partial_\tau \tilde{f}^n_h, \psi_h)_L + \frac{X}{UL}\left(G^n_h \frac{\partial \tilde{f}^n_h}{\partial \ell}, \psi_h\right)_L = 0, \tag{12}$$

for all $\psi_h \in Q_{0,h}$. Here, the discrete form of the growth rate is defined as $G^n_h := G(\tilde{\rho}^n_{c,h}, \tilde{\vartheta}^n_h)$, and it is treated implicitly. Further, the inner product in $L^2(\Omega_{L,h})$ is denoted by $(\cdot,\cdot)_L$. In order to decouple the equations in (12), we use an iteration of fixed point type. The fixed point iteration for the coupled ordinary and partial differential equations in (12) reads:

Let $\tilde{\vartheta}^{n_0}_h = \hat{\vartheta}^n_h$, $\tilde{\rho}^{n_0}_{c,h} = \hat{\rho}^n_{c,h}$, $\tilde{f}^{n_0}_h = \hat{f}^n_h$ and $G^{n_k}_h := G(\tilde{\rho}^{n_k}_{c,h}, \tilde{\vartheta}^{n_k}_h)$, then solve

$$(\partial_\tau \tilde{f}^{n_k}_h, \psi_h)_L + \frac{X}{UL}\left(G^{n_{k-1}}_h \frac{\partial \tilde{f}^{n_k}_h}{\partial \ell}, \psi_h\right)_L = 0,$$

$$\partial_\tau \tilde{\vartheta}^{n_k}_h - H^\vartheta_{gr}(\tilde{\vartheta}^{n_{k-1}}_h, \tilde{\rho}^{n_{k-1}}_{c,h}, \tilde{f}^{n_k}_h) = 0,$$

$$\partial_\tau \tilde{\rho}^{n_k}_{c,h} - H^\rho_{gr}(\tilde{\vartheta}^{n_k}_h, \tilde{\rho}^{n_{k-1}}_{c,h}, \tilde{f}^{n_k}_h) = 0, \tag{13}$$

for $k = 1, 2, \ldots$, until the residual of each equation in (13) become less than 10^{-8}. Then, we set $\tilde{f}^n_h = \tilde{f}^{n_k}_h$, $\vartheta^n_h = \tilde{\vartheta}^{n_k}_h$ and $\rho^n_{c,h} = \tilde{\rho}^{n_k}_{c,h}$. This iterative procedure is inexpensive and usually satisfies the residual condition within two or three iterations. Finally, we construct the global discrete solution

$$f^n_h(\mathbf{x}, \ell) = \left\{ \sum_{j=1}^{\mathcal{M}} \sum_{l=1}^{\mathcal{N}} f^n_{j,l} \phi_j(\mathbf{x}) \psi_l(\ell) \right\} \in V_h \otimes Q_h,$$

by setting $f^n_{j,l} = \tilde{f}^n_{j,l}$, and use it as the initial solution for (11) in the next time step.

Remark 1. The inclusion of the source–sink term, which accounts for the aggregation, agglomeration and breakage phenomena, in the L-direction PBE (12) is straightforward.

Remark 2. Although only a size independent growth rate is considered in the model, the proposed numerical scheme is not restricted to this case. In particular, the growth rate in (12) can be a function of particle size.

Remark 3. Note that the error induced in (11) and (12) by the operator-splitting method is of order τ^2 for the backward Euler scheme, see Ganesan and Tobiska (2011).

3.3. *Parallel implementation of the operator-splitting finite element method*

In each time step, we first solve the system of partial differential equations in the splitting step 1. Then, the set of solutions are communicated from X-direction (step 1) to the L-direction (step 2). Finally, we solve the system of coupled ordinary and partial differential equations in step 2. In this solution process, an efficient numerical procedure is needed to communicate the solution from the X-direction to the L-direction and vice verse. Two variants of fully practical algorithms for an operator-splitting finite element method have been presented in Ganesan and Tobiska (2011). It has been shown that the nodal point based algorithm is more efficient. Here, we first briefly recall the nodal point based operator-splitting algorithm and then present a parallel implementation of this algorithm.

Let $\hat{f}^n_{j,l}$, $j = 1, \ldots, \mathcal{M}$, and $\tilde{f}^n_{j,l}$, $l = 1, \ldots, \mathcal{N}$, be the set of nodal functionals of the finite element functions $\hat{f}^n_h \in V_h$, and $\tilde{f}^n_h \in Q_h$, respectively, at the time step t^n, *i.e.*,

$$\hat{f}^n_h(\mathbf{x}, \ell_l) = \sum_{j=1}^{\mathcal{M}} \hat{f}^n_{j,l} \phi_j(\mathbf{x}), \quad \tilde{f}^n_h(\mathbf{x}_j, \ell) = \sum_{l=1}^{\mathcal{N}} \tilde{f}^n_{j,l} \psi_l(\ell).$$

Here, ℓ_l, $l = 1, \ldots, \mathcal{N}$ are the L-coordinate Cartesian points (nodal points) which are necessary to evaluate the nodal functionals $\tilde{f}^n_{j,l}$. Similarly, $\mathbf{x}_j$, $j = 1, \ldots, \mathcal{M}$ are the X-coordinate Cartesian points which are necessary to evaluate the nodal functionals $\hat{f}^n_{j,l}$. In the above finite element function definition, the nodal functionals are defined as point values of the function, and in this case $\tilde{f}^n_{j,l} = \hat{f}^n_{l,j}$. Alternatively, the nodal functionals can also be defined by weighted integral values on each cell, and in this case the number of nodal points is equal to the sum of the number of quadrature points used to evaluate the weighted integral in all cells. To fix the notation, we assume that the nodal functionals are defined by point values. Further, let us consider a simple case, *i.e.*, 1D in X-direction and 1D in L-direction, and assume that there are four and five nodal points in X- and L-directions, respectively. The top and bottom pictures in Fig. 2 represent the solution direction in the operator-splitting steps. In the solution process, we first solve a set of five 1D X-direction equations, *i.e.*, we solve 1D X-direction equations for each nodal point ℓ_l of $\tilde{f}^n_h \in Q_h$. Then, we transpose the solution $\tilde{f}^n_{j,l}$ to get $\tilde{f}^n_{j,l}$, which is needed to assemble the right-hand side of the L-direction equations. Finally, in step 2 we solve a set of four 1D L-direction equations, *i.e.*, we solve 1D L-direction equations for each nodal point $\mathbf{x}_j$ of $\hat{f}^n_h \in V_h$. Since the nodal functionals of $\hat{f}^n_h$ are defined by point values, assembling the right

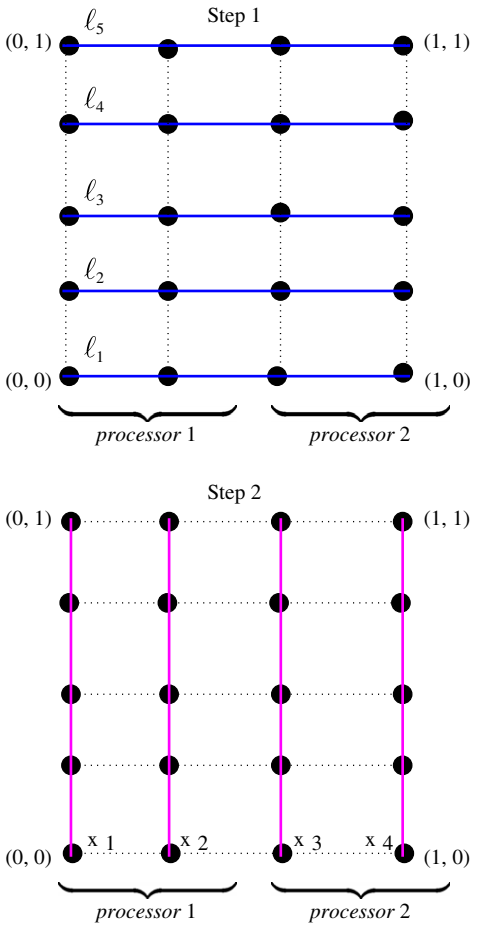

Fig. 2. Representation of X- and L-directions (top and bottom, respectively) solution processes in the operator-splitting method. The solid and dotted lines represent the direction of the active and inactive operators, respectively.

hand side of the population balance equation in (12), is just a matrix–vector multiplication.

Next, we present the parallel implementation for the nodal point based operator-splitting algorithm. Assume that we have N number of processors. We first partition the collection of cells $\mathcal{T}_h$ of Ω_X into N number of sub-collections, $\mathcal{T}_{h,k}$, $k=0,1,\ldots,N-1$, using the Metis package (Karypis and Kumar, 1998). After that, in each processor we construct the local finite element space and assemble the local system matrix for all X-direction equations. Then, we call the external parallel direct solver MUMPS (Amestoy et al., 2001, 2006) from each processor, by providing their corresponding local system matrix, and obtain the X-direction solution for all L-direction levels ℓ_l.

In step 2 of the operator-splitting algorithm, in each processor k we first collect their own X-direction nodal points $\mathbf{x}_j$, which belongs to $\mathcal{T}_{h,k}$. Then, we solve a set of L-direction equations (12) in each processor for all X-direction nodal points $\mathbf{x}_j$ belonging to their processor. Note that the solution of L-direction equations (12) in each processor is independent of the solution in other processors. Thus, no communications between processors are needed in L-direction (step 2) solution process, and it facilitates an ideal speedup in parallel computing. In our algorithm, if an X-direction nodal point $\mathbf{x}_j$ belongs to two processors, that is, if $\mathbf{x}_j$ is on the boundary between two processors, then we prefer to solve Eqs. (12) for $\mathbf{x}_j$ on both processors. Alternatively, we could solve Eqs. (12) for $\mathbf{x}_j$ in one processor, and then communicate the solution to the other processor. Since the population balance equation in (12) is an 1D problem with very less number of degrees of freedom in our application problem, solving the population balance equation in (12) for $\mathbf{x}_j$ in each processor is more efficient than communication between processors.

Note that the values of the mass and stiffness matrices in the X-direction equation (11) does not vary over time. Therefore, we assemble and factorize the X-direction system matrix once at the beginning, and reuse the same LU factorization over time. Further, the system matrix of the X-direction equation (11) is same for all L-direction levels. Therefore, we solve the system with multiple right hand side to get the X-direction solution for all L-direction levels which is very efficient with the direct solver.

Also, note that the mass matrix of population balance equation in (12) is same for all X-direction nodal points. Therefore, we assemble it at the beginning and reuse it at every time step. Since the structure of the growth term matrix of population balance equation in (12) is same for all X-direction nodal points, we allocate the memory for it only once and reuse the same memory to assemble the growth term matrix for every X-direction nodal point. The obtained linear system for every X-direction nodal point is then solved by the direct solver UMFPACK (Davis, 2004a,b; Davis and Duff, 1999). Note that the growth term G depends on $\mathbf{x}\in\Omega_X$, otherwise we would have also reused the growth term matrix for all X-direction nodal points.

4. Numerical experiments

The operator-splitting finite element method applied to the PBS in the previous sections has been validated in Ganesan (2010) and Ganesan and Tobiska (2011) for a scalar problem with known analytical solution. Further, the computational results obtained for the PBS using the proposed numerical scheme have been used as the reference solution (snapshots) in Krasnyk et al. (in press-b) for constructing a reduced model.

Here, we study the effects of cooling on the crystal growth. In the considered model, liquid feed (supersaturated urea–ethanol solution) with seed crystals enter into the crystallizer. Then, the seed and nucleated crystals grow inside the crystallizer due to cooling. Finally, the mixture of liquid and crystals are continuously removed at the outlet of the crystallizer. The parameters used in our simulations are given in Table 1.

4.1. Initial and boundary conditions

In our simulations, a parabolic inlet velocity profile with $\overline{\mathbf{u}}_D=(1\times10^{-2}\ \mathrm{m/s},\ 0)$ is used. It results in $Re=73.46$ for the considered parameters. The considered initial values for the temperature and solute partial density are $\vartheta_0=301.15$ K and $\rho_{c_0}=71.9\ \mathrm{kg/m^3}$. Further, we assume that the crystallizer does not contain any crystal particles initially, that is, $f_0=0$. At the inlet, we imposed $\vartheta_D=301.15$ K and $\rho_{c_D}=71.9\ \mathrm{kg/m^3}$ as the boundary values for the temperature and solute partial density, respectively. An experimentally measured size distribution of the seed crystals is used as the inlet condition for f_D. Fig. 3 shows the partial size distribution of the seed crystals. These values result in $Pe_\vartheta=1153$, $Pe_c=74\,074$ and $Pe_x=1000$.

To study the effects of cooling on the crystal growth the following three cases are considered:

*Case*1: $\vartheta_{wall}=291.15$ K.
*case*2: $\vartheta_{wall}=295.15$ K.
*case*3: $\vartheta_{wall}=299.15$ K.
Further, simulations are performed until the dimensionless time $T=5000$ with the time step $\tau=0.1$ for all these cases.

Table 1
Ethanol properties at 25 °C.

$\mu=1.074\times10^{-3}$ (Pa s
$\rho=7.89\times10^{2}\ \mathrm{kg/m^3}$
$\lambda=0.167$ W/(m K)
$c_p=2.441\times10^{3}$ J/(kg K)
$h_{cr}=2.1645\times10^{5}$ J/kg
$D_c=1.35\times10^{-9}\ \mathrm{m^2/s}$
$\rho^d=1.323\times10^{3}\ \mathrm{kg/m^3}$
$k_V=\pi/6$, –
$k_g=1\times10^{-7}$ m/s
$g=0.5$, –
$D_x=1\times10^{-7}\ \mathrm{m^2/s}$
$\alpha_{nuc}=1\times10^{8}\ 1/(\mathrm{m^2\ s})$
$\beta_{nuc}=1.66667\times10^{-6}$, –
$U=1\times10^{-2}$ m/s
$X=1\times10^{-2}$ m
$L=1.69\times10^{-3}$ m
$f_{max}=1\times10^{10}\ 1/\mathrm{m^3}$
$\rho_{c,sat}=1.3045(\vartheta-273.15)+35.3642\ \mathrm{kg/m^3}$

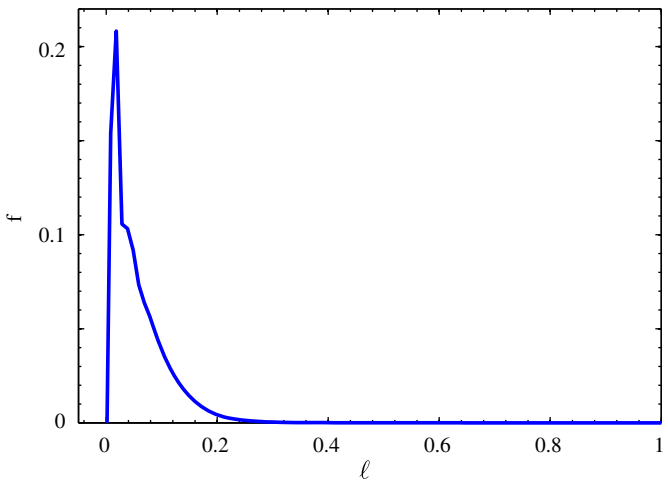

Fig. 3. Particle size distribution of the seed crystals.

4.2. Flow field

As mentioned earlier, we initially solve the stationary Navier–Stokes equations (1) once and reuse the fluid velocity in the scalar equations (2)–(4) over the period of time. The computational domain contains 23 040 quadrilateral cells, and the same mesh is used for all time-dependent scalar equations. For the spatial discretization of the Navier–Stokes equations, we use the LBB-stable finite element pair Q_2/P_1^{disc}, *i.e.*, piecewise continuous biquadratic and piecewise discontinuous linear finite elements for the velocity and the pressure, respectively (Matthies and Tobiska, 2002). The tangential and normal fluid velocity flow profiles obtained in our simulation are depicted in Fig. 4. Note that only the initial part of the channel (0.18 m from the inlet) is shown in the figure for better visibility.

4.3. Energy and mass balances

The energy and solute mass balance equations are spatial discretized using the piecewise continuous bilinear finite elements Q_1. It results in 23 569 degrees of freedom for each scalar equation. Further, the implicit backward Euler scheme is applied for the temporal discretization of these equations.

The development of the temperature profile over the time in case 1 is depicted in Fig. 5. Since the variation of the wall temperature among different cases is less, the development of the temperature profile is similar in all three cases. Thus, the temperature profiles of other cases are not presented here. Further, the steady state profile is reached after the dimensionless time $t=50$ in all three cases.

Next, the development of the solute partial density profile over the time in case 1 is presented in Fig. 6. Note that the liquid feed (supersaturated urea–ethanol solution) enters the crystallizer continuously and also we assumed that the crystallizer is filled with the liquid feed initially. Thus, the variation of the solute partial density in the crystallizer over time is very less, see the minimum and maximum values of ρ_c in Fig. 6. Again, note that only the initial part of the channel (0.18 m from the inlet) is shown in Figs. 5 and 6 for better visibility.

4.4. Particle size distribution

The same computational domain used for the energy and solute mass balance equations is again used for the PBE in X-direction. The L-direction 1D computational domain contains 40 line intervals. Further, the population balance equation in X- and L-directions are spatially discretized using the piecewise continuous bilinear Q_1 and the piecewise continuous linear P_1 finite elements, respectively. These result in 23 569 and 41 degrees of freedom for X- and L-direction population balance equations. Thus, in each time step

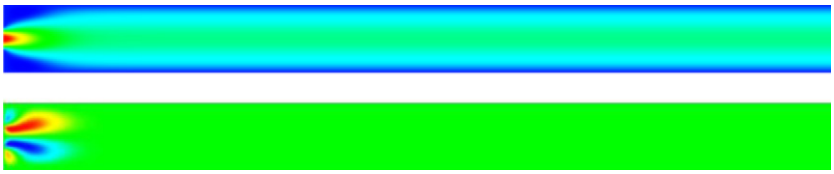

Fig. 4. The tangential (top) and normal (bottom) fluid velocity flow profiles near the inlet (0.18 m). The minimum (blue) and maximum (red) values in tangential component is 0.055 and 1.0, and in normal component is −0.0836 and 0.0836, respectively, (variables are scaled and dimensionless). (For interpretation of the references to color in this figure legend, the reader is referred to the web version of this article.)

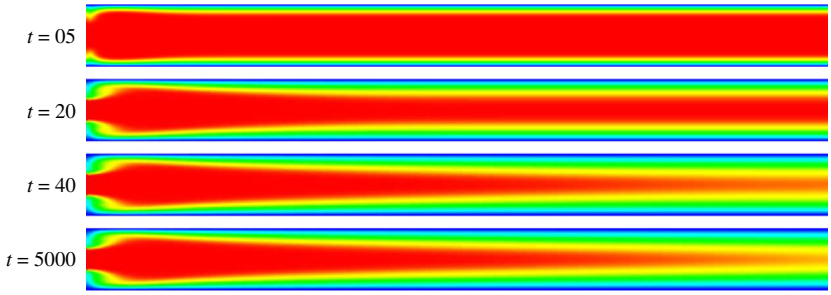

Fig. 5. Temperature profiles near the inlet (0.18 m) at $t=05$, 20, 40 for the case 1. The minimum (blue) and maximum (red) temperature values are 0.966 and 1.0, respectively, (variables are scaled and dimensionless). (For interpretation of the references to color in this figure legend, the reader is referred to the web version of this article.)

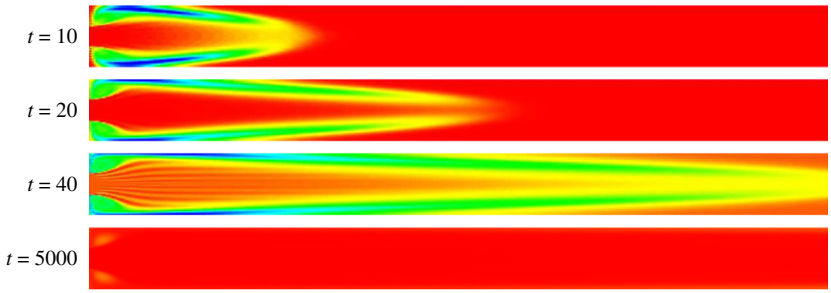

Fig. 6. Solute partial density profiles near the inlet (0.18 m) at $t=10$, 20, 40. The minimum (blue) and maximum (red) values are 0.99 and 1.0, respectively (variables are scaled and dimensionless). (For interpretation of the references to color in this figure legend, the reader is referred to the web version of this article.)

the total number of degrees of freedom used to approximate the population balance equation is 966 329.

Now, we present the steady state particle size distribution profile at the dimensionless time $t=5000$ for the considered cases. First, the steady state particle nucleation profile at L_{min} which is imposed as the Dirichlet boundary value on L_{min} in the L-direction step (10) is presented in Fig. 7. It is clear that there will be a low nucleation rate near the inlet, since the solution will be in supersaturated state. Further, there is no significant difference in the steady state nucleation rate among all three cases, since the variation in the wall temperature is less and the same flow velocity and inlet conditions are used.

Next, the computationally obtained steady state particle distribution profile in case 1 for different particle sizes are presented in Fig. 8. It can be clearly seen that the smaller particles of size $\ell=0.0132$ are more concentrated near the inlet. Due to the crystal growth, the particle size becomes larger when the residence time increases. Thus, the largest particles are found near the outlet, see the distribution of particles of size $\ell=0.1052$ in Fig. 8.

The steady state particle distribution profile obtained in the case 3 for different particle sizes are presented in Fig. 9. As we observed in the case 1, the smaller and the larger particles are found near the inlet and the outlet, respectively. Observe that the distributions of larger particle of size $\ell=0.1052$ in case 1 (bottom right in Fig. 8) and in case 3 (bottom right in Fig. 9). The distribution of larger particles near the outlet in case 1 are more than the distribution in case 3 due to higher cooling in case 1. Further, we would expect a higher value for the PSD (f) towards the wall, since the nucleation rate near the wall is high, see, Fig. 7. This behavior is not clearly visible in both Figs. 8 and 9, and the PSD along the x_2-coordinate looks nearly flat. This could be because of the following reasons: (i) the flow become well-mixed just after the inlet, since only the inlet region is shown in Fig. 7, and (ii) the maximum value of the nucleation rate is 0.01, see Fig. 7. However, near the outlet region, f is slightly large at the walls compared to the middle, see Fig. 10, which is plotted with different scaling. Also, due to higher cooling in case 1, f along the x_2-coordinate is more bend (near the outlet region) towards higher values at the wall than in case 3.

Finally, in our numerical study we evaluate the volume fraction q_3 of f using

$$q_3(t,\mathbf{x},\ell)=\frac{\ell^3 f(t,\mathbf{x},\ell)}{\int_{L_{min}}^{L_{max}}\ell^3 f(t,\mathbf{x},\ell)\,d\ell}.$$

The evaluated volume fractions with respect to the particle size for different positions and cases are presented in Fig. 11. The volume fraction of the time independent inlet particle size distribution evaluated at $\mathbf{x}=(0,0.5)$ is denoted as var 0 in the figure, whereas the var 1, 2 and 3 in the figure represent the volume fractions evaluated near the outlet at $\mathbf{x}=(190,0.5)$ and $t=5000$ for the cases 1, 2 and 3, respectively. Small fluctuations in the volume fraction of the experimental data can be seen in var 0 (left), but it is not clearly visible in the PSD plot (Fig. 3) due to scaling. A higher cooling will increase the nucleation and growth rates, and therefore the volume fraction of large size particles will be more in higher cooling cases. This behavior can be seen in the magnified Fig. 11 (right), in which the plotted curves correspond piecewise linear interpolations of seven computed volume fractions.

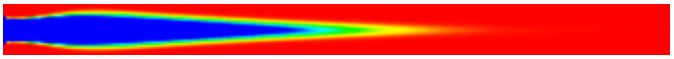

Fig. 7. Steady state nucleation profile ($f=B_{nuc}/(Gf_{max})$ at L_{min}) near the inlet (0.18 m) at $t=5000$. The minimum (blue) and maximum (red) values are 0 and 0.01, respectively (variables are scaled and dimensionless). (For interpretation of the references to color in this figure legend, the reader is referred to the web version of this article.)

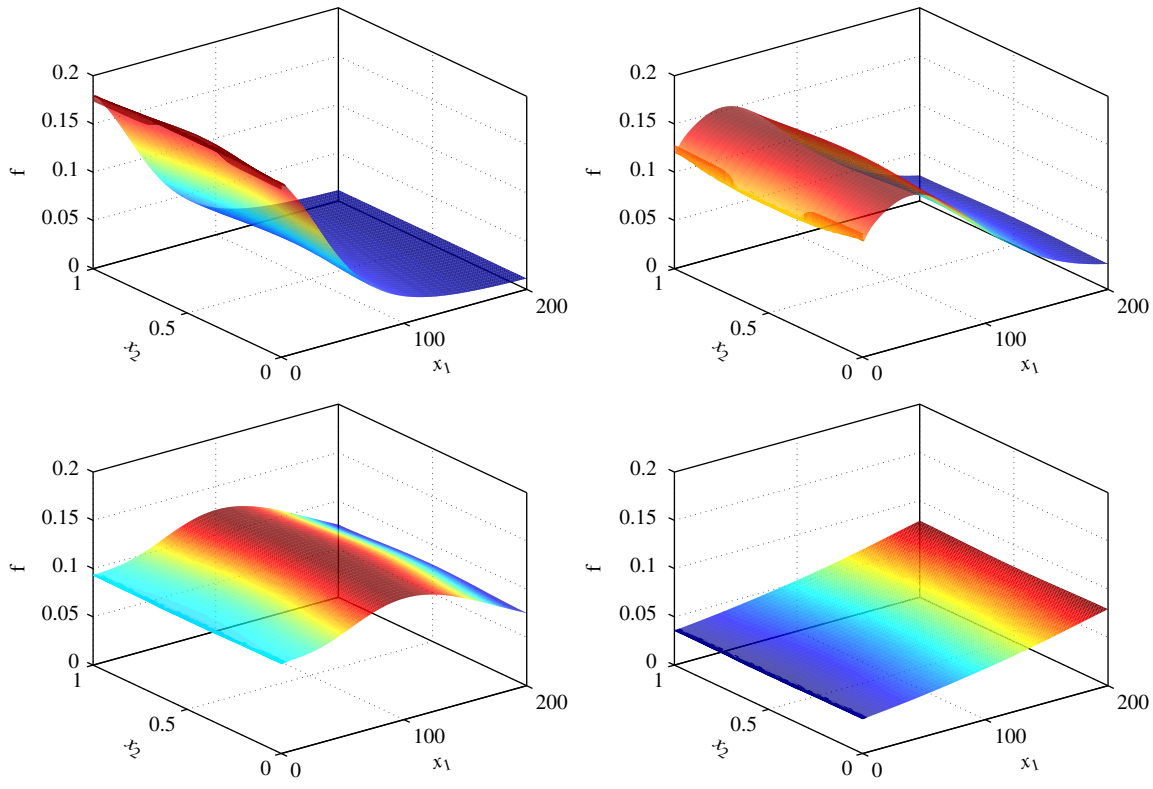

Fig. 8. Computationally obtained steady state (at $t=5000$) particle size distribution f of particle size $\ell=0.0132$ (top left), $\ell=0.0277$ (top right), $\ell=0.048$ (bottom left) and $\ell=0.1052$ (bottom right) with $T_{wall}=291.5$ K (case 1).

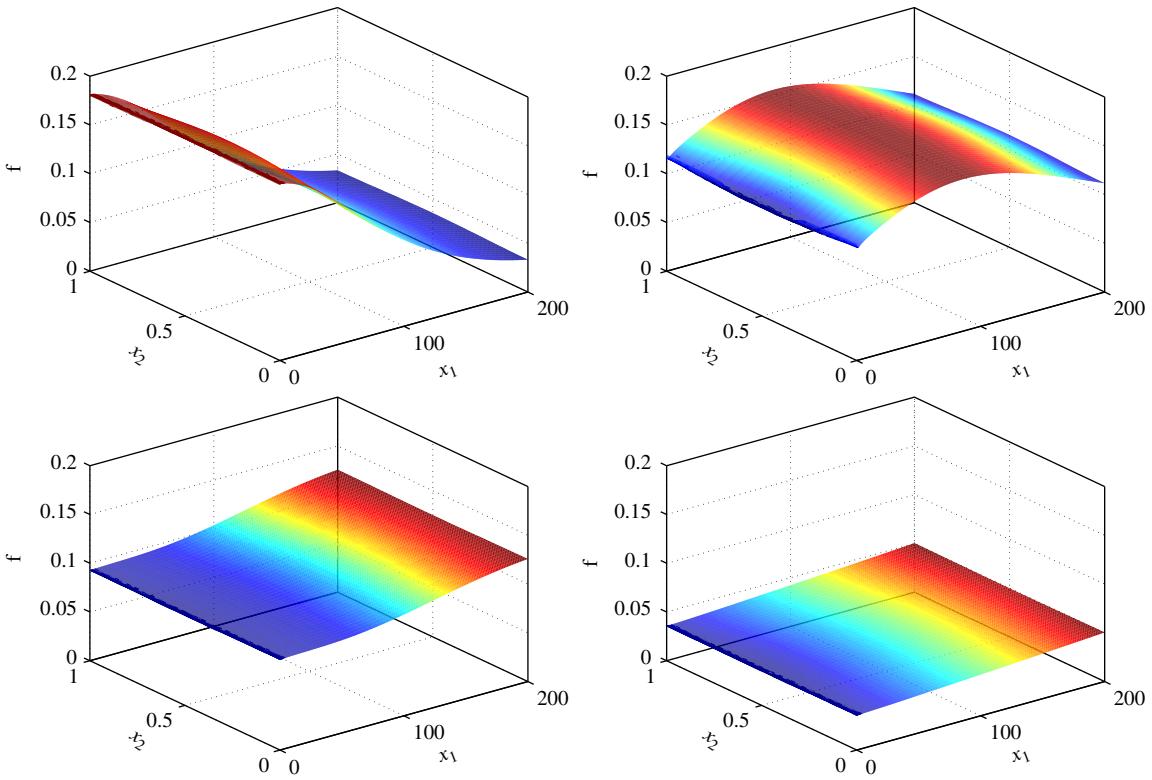

Fig. 9. Computationally obtained steady state (at $t=5000$) particle size distribution f of particle size $\ell=0.0132$ (top left), $\ell=0.0277$ (top right), $\ell=0.048$ (bottom left) and $\ell=0.1052$ (bottom right) with $T_{wall}=299.15$ K (case 3).

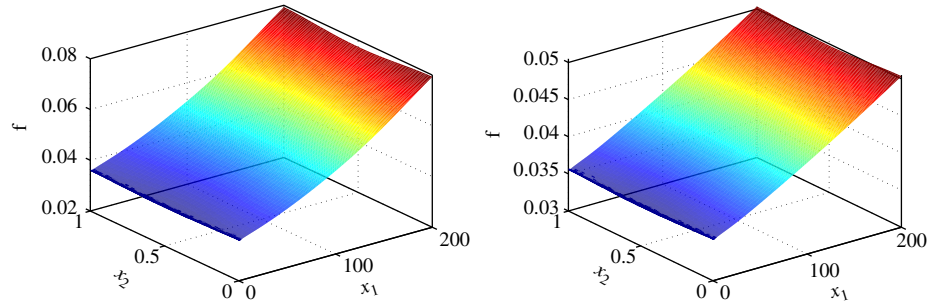

Fig. 10. Computationally obtained steady state (at $t=5000$) particle size distribution f of particle size $\ell=0.1052$ in case 1 (left) and case 3 (right).

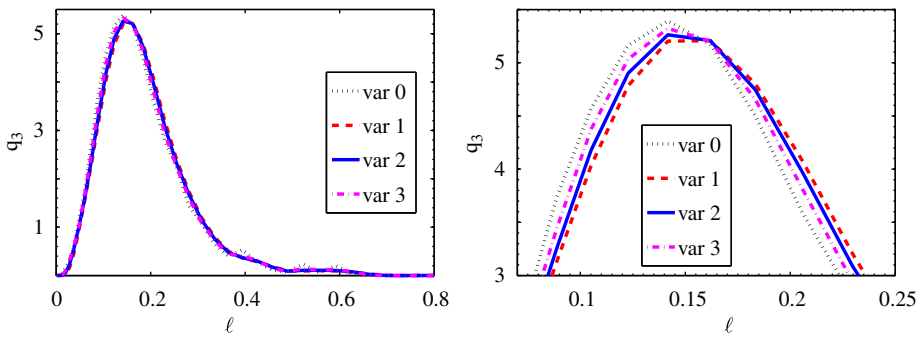

Fig. 11. The evaluated volume fractions of f at different positions and cases, magnified view on the right side. The inlet volume fraction, var 0: $\mathbf{x}=(0,0.5)$ whereas var 1, 2 and 3 are volume fractions of cases 1, 2 and 3, respectively, evaluated near the outlet at $\mathbf{x}=(190,0.5)$ at time $t=5000$.

4.5. Computational cost

The considered test example does not require an extensive parallel computing, since the number of degrees of freedom (spatial) used to solve each scalar equation is 23 569. The number of degrees is significantly less to study the speed-up on a distributed memory parallel implementation (MPI implementation) due to communication overhead. However, to illustrate the parallel implementation, simulations are performed using seven Intel(R) Xeon(R) processors with 2.932 GHz each. In each time

step, the total number of degrees of freedom used to approximate the coupled system of 2D scalar equations (2), (3) and the 3D PBE (4) is 1 013 467. Despite the considerably large number of total degrees of freedom, the required computing time with seven processors is only 1.4 s per time step. We expect the proposed finite element algorithm will provide a good speed-up for PBS in $\mathbb{R}^{3+s}$, $s \geq 1$ and it will be studied intensively in our future work.

5. Summary

An operator-splitting finite element method is presented for multidimensional population balance equations coupled with equations of conservation of mass, momentum and energy. Using a dimensional splitting, the multidimensional PBE is split into spatial and internal PBEs, which contain only derivatives with respect to spatial and internal coordinates, respectively. Furthermore, the splitting is also applied to the coupling terms in the scalar energy and mass balance equations. It facilitates to apply decoupling iterations between a set of ordinary and internal population balance equations. The proposed finite element scheme allows 'arbitrary' spatial domains and is not restricted to rectangular or brick type domains in $\mathbb{R}^d$, $d=2$ or $d=3$. This results from the fact that the dimensional splitting is only applied to separate spatial and internal coordinates. The operator-split spatial PBE together with the energy and mass balance equations are solved by finite elements using the same spatial mesh, whereas a separate 1D mesh is used for the finite element solution of the internal PBE. A nodal point based operator-splitting finite element algorithm is presented for the communication of the solution between the spatial and internal population balance equations. Moreover, parallel algorithms are implemented by decomposing the spatial domain, that is, without decomposing the internal domain. This, avoids any special algorithm to handle improper load balance in the evaluation of aggregation and breakage integral terms, which have varying computational cost across the internal mesh cells.

Simulations of a crystallization process, which occur due to cooling, in a 2D channel are performed using the proposed finite element scheme. A set of computational results are presented for different wall temperatures and showed the effects of the cooling on the crystal growth. The computing time in each time step for the solution of 3D PBE coupled with the 2D energy and mass balance equations using seven processors and 1 013 467 total number of degrees is less than 1.4 s. In our simulations only a size independent crystal growth is considered. However, the inclusion of a size dependent crystal growth, of agglomeration and breakage phenomena in the finite element scheme is possible. Further, the proposed finite element scheme for PBS's in $\mathbb{R}^{2+1}$ can be extended to PBS's in $\mathbb{R}^{3+s}$, $s \geq 1$ which will be the topic of future work.

Acknowledgment

This work has been supported by the Alexander von Humboldt (AvH) foundation, Germany and the Federal Ministry of Education and Research (BMBF), Germany.

References

Amestoy, P.R., Duff, I.S., Koster, J., L'Excellent, J.Y., 2001. A fully asynchronous multifrontal solver using distributed dynamic scheduling. SIAM J. Matrix Anal. Appl. 23, 15–41.

Amestoy, P.R., Guermouche, A., L'Excellent, J.Y., Pralet, S., 2006. Hybrid scheduling for the parallel solution of linear systems. Parallel Comput. 32, 136–156.

Borchert, C., Sundmacher, K., 2011. Crystal aggregation in a flow tube: image-based observation. Chem. Eng. Technol. 34, 545–556.

Braatz, R.D., 2002. Advanced control of crystallization processes. Annu. Rev. Control 26, 87–99.

Chang, C., Powell, R.L., 2002. Hydrodynamic transport properties of concentrated suspensions. AIChE J. 48, 2475–2480.

Chen, P., Sanyal, J., Dudukovic, M., 2004. CFD modeling of bubble columns flows: implementation of population balance. Chem. Eng. Sci. 59, 5201–5207.

Costa, C.B.B., Maciel, M.R.W., Filho, R.M., 2007. Considerations on the crystallization modeling: population balance solution. Comput. Chem. Eng. 31, 206–218.

Davis, T.A., 2004a. Algorithm 832: UMFPACK V4.3—an unsymmetric-pattern multifrontal method. ACM Trans. Math. Software 30, 196–199.

Davis, T.A., 2004b. A column pre-ordering strategy for the unsymmetric-pattern multifrontal method. ACM Trans. Math. Software 30, 167–195.

Davis, T.A., Duff, I.S., 1999. A combined unifrontal/multifrontal method for unsymmetric sparse matrices. ACM Trans. Math. Software 25, 1–20.

Ganesan, S., 2010. An operator-splitting heterogeneous finite element method for population balance equations: stability and convergence. Preprint 1531. WIAS, Berlin.

Ganesan, S., Tobiska, L., 2011. Implementation of an operator-splitting finite element method for high-dimensional parabolic problems. Preprint 04-11. Otto-von-Guericke-Universität Magdeburg, Fakultät für Mathematik.

Gunawan, R., Fusman, I., Braatz, R.D., 2004. High resolution algorithms for multidimensional population balance equations. AIChE J. 50, 2738–2749.

Gunawan, R., Fusman, I., Braatz, R.D., 2008. Parallel high-resolution finite volume simulation of particulate processes. AIChE J. 54, 1449–1458.

Hackbusch, W., John, V., Khachatryan, A., Suciu, C. A numerical method for the simulation of an aggregation-driven population balance system. Int. J. Numer. Methods Fluids, doi: 10.1002/fld.2656. In press.

Hulburt, H., Katz, S., 1964. Some problems in particle technology: a statistical mechanical formulation. Chem. Eng. Sci. 19, 555–574.

John, V., Roland, M., 2010. On the impact of the scheme for solving the higher-dimensional equation in coupled population balance systems. Int. J. Numer. Methods Eng. 82, 1450–1474.

John, V., Roland, M., Mitkova, T., Sundmacher, K., Voigt, L.T.A., 2009. Simulations of population balance systems with one internal coordinate using finite element methods. Chem. Eng. Sci. 64, 733–741.

Karypis, G., Kumar, V., 1998. METIS—A Software Package for Partitioning Unstructured Graphs, Partitioning Meshes, and Computing Fill-Reducing Orderings of Sparse Matrices. Version 4.0. University of Minnesota.

Krasnyk, M., Borchert, C., Mangold, M. Model reduction techniques for the simulation of particle populations in fluid flow. Mathematical and Computer Modelling of Dynamical Systems. In press-a.

Krasnyk, M., Mangold, M., Ganesan, S., Tobiska, L. Numerical reduction of a crystallizer model with internal and external coordinates by proper orthogonal decomposition. Chem. Eng. Sci., doi: 10.1016/j.ces.2011.05.053. In press-b.

Lian, G., Moore, S., Heeney, L., 2006. Population balance and computational fluid dynamics modelling of ice crystallisation in a scraped surface freezer. Chem. Eng. Sci. 61, 7819–7826.

Ma, D.L., Tafti, D.K., Braatz, R.D., 2002a. High-resolution simulation of multidimensional crystal growth. Ind. Eng. Chem. Res. 41, 6217–6223.

Ma, D.L., Tafti, D.K., Braatz, R.D., 2002b. Optimal control and simulation of multidimensional crystallization processes. Comput. Chem. Eng. 26, 1103–1116.

Majumder, A., Kariwala, V., Ansumali, S., Rajendran, A., 2010. Fast high-resolution method for solving multidimensional population balances in crystallization. Ind. Eng. Chem. Res. 49, 3862–3872.

Matthies, G., Tobiska, L., 2002. The inf–sup condition for the mapped Q_k/P_{k-1}^{disc} element in arbitrary space dimensions. Computing 69, 119–139.

Pinto, M.A., Immanuel, C.D., III, F.J.D., 2008. A two-level discretisation algorithm for the efficient solution of higher-dimensional population balance models. Chem. Eng. Sci. 63, 1304–1314.

Qamar, S., Ashfaq, A., Warnecke, G., Angelov, I., Elsner, M., Seidel-Morgenstern, A., 2007. Adaptive high-resolution schemes for multidimensional population balances in crystallization processes. Comput. Chem. Eng. 31, 1296–1311.

Qamar, S., Noor, S., Rehman, M., Seidel-Morgenstern, A., 2011. Numerical solution of a multi-dimensional batch crystallization model with fines dissolution. Comput. Chem. Eng. 35, 412–422.

Ramkrishna, D., 2000. Population Balances, Theory and Applications to Particulate Systems in Engineering. Academic Press, San Diego.

Ramkrishna, D., Mahoney, A.W., 2002. Population balance modeling. Promise for the future. Chem. Eng. Sci. 57, 595–606.

Teipel, U., 2004. Particle technology: Design of particulate products and dispersed systems. Chem. Eng. Technol. 27, 751–756.

Woo, X.Y., Tan, R.B.H., Braatz, R.D., 2009. Modeling and computational fluid dynamics-population balance equation-micromixing simulation of impinging jet crystallizers. Cryst. Growth Des. 9, 156–164.

Woo, X.Y., Tan, R.B.H., Chow, P.S., Braatz, R.D., 2006. Simulation of mixing effects in antisolvent crystallization using a coupled CFD–PDF–PBE approach. Cryst. Growth Des. 6, 1291–1303.